19

Irradiation Effects on EUV Nanolithography Collector Mirrors

J.P. Allain
Purdue University
United States of America

1. Introduction

Exposure of collector mirrors facing the hot, dense pinch plasma in plasma-based EUV light sources to debris (fast ions, neutrals, off-band radiation, droplets) remains one of the highest critical issues of source component lifetime and commercial feasibility of nanolithography at 13.5-nm. Typical radiators used at 13.5-nm include Xe, Li and Sn. Fast particles emerging from the pinch region of the lamp are known to induce serious damage to nearby collector mirrors. Candidate collector configurations include either multi-layer mirrors (MLM) or single-layer mirrors (SLM) used at grazing incidence. Due to the strong absorbance of 13.5-nm light only reflective optics rather than refractive optics can work in addition to the need for ultra-high vaccum conditions for its transport.

This chapter presents an overview of particle-induced damage and elucidates the underlying mechanisms that hinder collector mirror performance at 13.5-nm facing high-density pinch plasma. Results include recent work in a state-of-the-art in-situ EUV reflectometry system that measures real time relative EUV reflectivity (15-degree incidence and 13.5-nm) variation during exposure to simulated debris sources such as fast ions, thermal atoms, and UV radiation (Allain et al., 2008, 2010). Intense EUV light and off-band radiation is also known to contribute to mirror damage. For example off-band radiation can couple to the mirror and induce heating affecting the mirror's surface properties. In addition, intense EUV light can partially photoionize background gas used for mitigation in the source device. This can lead to local weakly ionized plasma creating a sheath and accelerating charged gas particles to the mirror surface inducing sputtering. In this overview we will also summarize studies of thermal and energetic particle exposure on collector mirrors as a function of temperature simulating the effects induced by intense off-band and EUV radiation found in EUVL sources. Measurements include variation of EUV reflectivity with mirror damage and in-situ surface chemistry evolution.

In this chapter the details from the EUV radiation source to the collector mirror are linked in the context of mirror damage and performance (as illustrated in Figure 1). The first section summarizes EUV radiation sources and their performance requirements for high-volume manufacturing. The section compares differences between conventional discharge plasma produced (DPP) versus laser plasma produced (LPP) EUV light sources and their possible combinations. The section covers the important subject of high-density transient plasmas and their interaction with material components. The different types of EUV radiators, debris

distribution, and mitigation sources are outlined. The second section summarizes the various optical collector mirror geometries used for EUV lithography. A brief discussion on the intrinsic damage mechanisms linked to their geometry is included. The third section summarizes in general irradiation-driven mechanisms as background for the reader and its relation to the "quiescent" plasma collector mirrors are exposed in EUV sources. This includes irradiation-driven nanostructures, sputtering, ion mixing, surface diffusion, and ion-induced surface chemistry. The fourth section briefly discusses EUV radiation-driven plasmas as another source of damage to the mirror. These plasmas are a result of using gases for debris mitigation. The fifth section is a thorough coverage of the key irradiation-driven damage to optical collector mirrors and their performance limitations as illustrated in part by Figure 1.

2. EUV radiation sources

There are numerous sources designed to generate light at the extreme ultraviolet line of 13.5-nm. Historically advanced lithography has considered wavelength ranges from hard X-rays up to 157 nm [Bakshi, 2009]. Radiators of 13.5-nm light rely on high-density plasma generation typically based on discharge-produced configurations with magnetically confined high-density plasmas or laser-produced plasmas. Recently, some sources have combined both techniques (Banine 2011). Generation of high-density plasmas to yield temperatures of the order of 10-50 eV require advanced materials for plasma-facing components in these extreme environments in particular discharge-produced plasma (DPP) configurations. This is due to the need of metallic anode/cathode components operating under high-heat flux conditions. Laser-produced plasmas (LPP) benefits from the fact that no nearby electrodes are necessary to induce the plasma discharge. Further details will be described in section 5.1. One challenge in operating EUV lamps at high power is the collected efficiency of photons at the desired exposure wavelength of 13.5-nm. This particular line has a number of radiators with properties that have consequences on EUV source operation. For example radiators at 13.5-nm include xenon, tin and lithium. The latter two are metals and thus their operation complicated by contamination issues on nearby material components such as electrodes and collector mirrors. Further discussion follows in section 2.2 and 2.3. To contend with the various types of debris that are generated in the plasma-producing volume a variety of novel debris mitigation systems (DMS) have been designed and developed for both DPP and LPP configurations.

2.1 Function and material components

The transient nature of the high-density plasma environment in DPP and LPP systems results in exposure of plasma-facing components to extreme conditions (e.g. high plasma density (~ 10^{19} cm^{-3}) and temperature (~ 20-40 eV). However, in LPP systems since the configuration is mostly limited by the mass of the radiator and the laser energy supplied to it to generate highly ionized plasma with the desired 13.5-nm light. Both configurations rely on efficient radiators of 13.5-nm light, which include: Li, Sn and Xe. In DPP designs a variety of configurations have been used that include: dense plasma focus, capillary Z-pinch, star pinch, theta pinch and hollow cathode among others. For a more formal description of these high-density plasma sources for 13.5-nm light generation the author refers to the recent publications by V. Bakshi in 2006 and 2009 (Bakshi, 2006; Bakshi, 2009).

The in-band and off-band radiation generated in these sources is also a critical limitation in operation of these lamps since on average the off-band radiation is converted into heat on nearby plasma-facing components. There are additional challenges in the design of 13.5-nm light sources that include: high-frequency operation limits driven by the need to extract high EUV power at the intermediate focus (IF) and limited by the available high-throughput power of the plasma device (e.g. laser system or discharge electrode system). Additionally, the scaling of debris with EUV power extraction and the limitation of conversion efficiency (CE) with source plasma size also translate into significant engineering challenges to the design of 13.5-nm lithography source design. Figure 1 illustrates, for the case of the DPP configuration, the primary debris-generating sources that compromise 13.5-nm collector mirrors. The first region depicted on the left is defined here as the "transient plasma region". This is the region described earlier with high-density and high-temperature plasma interacting with the electrode surfaces.

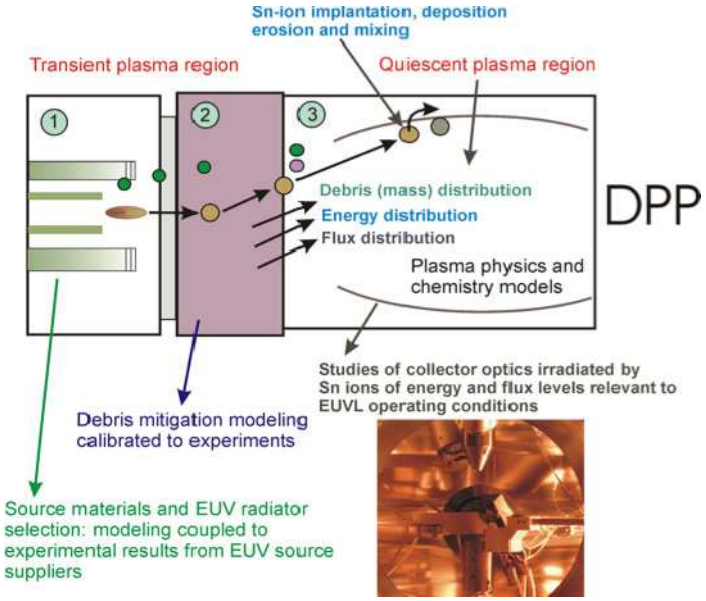

Fig. 1. Illustration of the various components of EUV 13.5-nm radiation source configuration consisting primarily of three major components: 1) plasma radiator section, 2) debris mitigation system and 3) optical collector mirror.

In DPP discharge sources material components that make up the electrode system consist of high-temperature, high-toughness materials. Although DPP source design has traditionally used high-strength materials such as tungsten and molybdenum alloys, the extreme conditions in these systems limit the operational lifetime of the electrode. Significant plasma-induced damage is found in the electrode surfaces, which induce degradation and abrasion over time. Figure 2, for example, shows a scanning electron micrograph of a tungsten electrode exposed to a dense plasma focus high-intensity plasma discharge. The key feature in the SEM image is the existence of plasma-induced damage domains that effectively have induced melting in certain sections of the electrode surface.

The second region depicted in Figure 1 is defined as the debris mitigation zone (DMZ). In this region a variety of debris mitigation strategies can be used to contend with the large debris that exists in operation of the DPP source. For example the use of inert gas to slow-down energetic particles that are generated in the pinch plasma region and/or debris mitigation shields that collect macro-scale particulates when using Sn-based radiators in DPP devices. Radiation-induced mechanisms on the surfaces of the DMZ elements also can lead to ion-induced sputtering of DM shield material that eventually is deposited in the nearby 13.5-nm collector mirror. Therefore care is taken to select sputter-resistant materials for the DM shields used such as refractory metal alloys and certain stainless steels. Design of DM shields also involve computational modeling that can aid in identifying appropriate materials depending on the source operation and generation of a variety of debris types such as clusters, ions, atoms, X-rays, electrons and macroscopic dust particles.

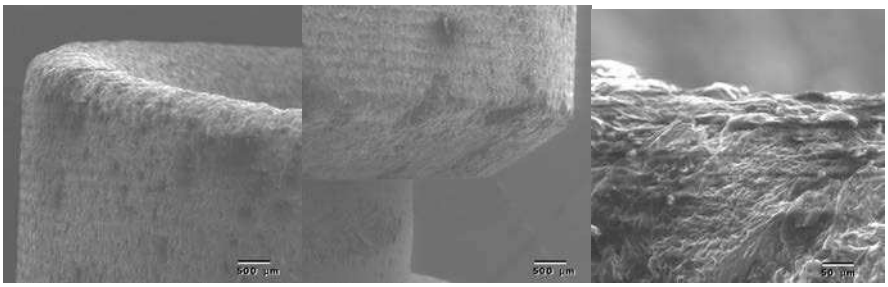

Fig. 2. SEM micrographs of a tungsten electrode exposed to high-intensity plasma during the generation of EUV 13.5-m light.

The third region in Fig. 1 consists of the 13.5-nm light collector mirror. The collector mirror has a configuration to optimally collect as much of the 13.5-nm light as possible. Its function is to deliver EUV power in a specified etendue at the intermediate focus (IF) or the opening of the illuminator. This power is in turn dictated by the specification on EUV exposure of the EUV lithography scanner that must be able to operate with 150-200 wafers per hour (wph) at nominal power for periods of 1-2 years without maintenance (so-called high-volume manufacturing, HVM, conditions). This ultra-stringent requirement is one of the primary challenges to EUV lithography today. Since powers of order 200-300 W at the IF need to be sustained for a year or more, materials at the DPP source and those used for collector mirrors will necessarily require revolutionary advances in materials performance. The third region in Figure 1 also depicts what debris the collector mirror is exposed to during the discharge. A distribution of debris energies (i.e. ions), fluxes and masses will effectively affect the mirror surface performance. The third region is also known as the "condenser or collector optics region".

2.2 Selection of electrode materials in DPP EUV devices

Selection of materials for DPP electrodes depends on the microstructure desired to minimize erosion and maximize thermal conductivity. Figure 3 shows an example of SEM micrographs of materials identified to have promising EUV source electrode properties. The powder composite materials inherited the structural characteristics of the initial powders, determined by the processes of combined restoration of tungsten and nickel oxides (WO_3

and NiO from $NiCO_3$, for instance) and copper molybdate ($MoCuO_4$). Dry hydrogen (the dew point temperature is above 20 ^{0}C) facilitates the formation of the heterogeneous conglomerates in W-Ni-powders, which do not collapse at sintering or saturate the material (Figure 3a), and spheroidizing of molybdenum particles and re-crystallization through the liquid phase in the conditions of sintering the composite consisting of molybdenum and copper (Figure 3b). For comparison, the structure is shown in Figure 3c obtained from tested W-Ni powders. The structure of the materials was studied by means of scanning electron microscopy (SEM) of the secondary electrons. A variety of materials characterization including surface spectroscopy and X-ray based diffraction is used to assess the condition of the materials after processing with sintering-based techniques. The powder composite materials are so-called pseudo alloys, which provide promising high thermal conductivity properties, while displaying sub-unity sputter yields (see Section 4).

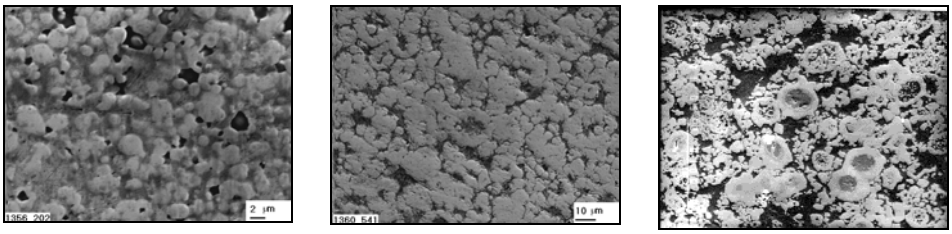

Fig. 3. From left to right, (a) the structure of the W-Cu-Ni-LaB6 pseudo alloy (x540), (b) the structure of the Cu-44%Mo – 1%LaB6 pseudo alloy (x2000), and (c) the structure of "irradiated" W-Cu-Ni pseudo alloy produced by class W-Ni powder (x400).

Observations made with secondary mass ion spectrometry (SIMS) on these materials found evidence of hydrogen and beryllium in anode components. Based on these results one can speculate that the hydrogen observed by SIMS after exposing the samples may be caused by that environment, in which the powders are manufactured, sintered, and additionally annealed. In regards to the beryllium observed on the anode surface after exposure to the xenon plasma, one may suppose two possible explanations, each of which requires additional verification. The construction may contain beryllium bronze; or the construction may contain Al_20_3 or BeO based ceramics. Both cases may be the reason for enrichment of the surface samples by these elements during the heating phases.

For systems with the absence of the component interactions, the arc xenon plasma impact to the electrode materials does not cause a noticeable change of durability: for $MoCuLaB_6$: HV = 1600-1690 MPa; and for Cu- Al_2O_3: HV = 660 MPa through the whole height of the anode. In the tungsten and copper based composites, when presence of nickel exists, the mutual dissolution of the elements is increased (W is dissolved in Cu-Ni melt, for instance). At cooling, it may be accompanied by either forming non-equilibrium solid solution, or solidification; which is conformed by the increasing the firmness of the upper part of the anode (3380 MPa compared to 3020 MPa in its lower part). To provide more careful analysis, one should investigate the dependence of electro-conductive composites on heat resistance subject to arc discharges of powerful heat fluxes (up to 10^7 W/m^2). Additional analyses typically conducted include the propagation of cracks, observed on the surface layer of the anode material and deep into the bulk. For that, the precise method of manufacturing is required for further insight on crack development and

propagation. These analyses along with erosion material modeling (discussed in Section 4) are mainly used to dictate materials selection for electrode materials in EUV DPP sources.

2.3 EUV radiators, debris generation and debris mitigation systems

One particularly important "coupling" effect between the debris mitigation zone region and the collector optics region is the use of inert mitigation gases (e.g. Ar or He) that in turn are ionized by the expanding radiation field and thus generate low-temperature plasma near the collector mirror surface. This phenomenon is briefly discussed in Section 3. Each candidate radiator (e.g. Li, Sn or Xe or any combination) will result in a variety of irradiation-induced mechanisms at the collector mirror surface. For example, if one optimizes the EUV 13.5-nm light source for Li radiators, the energy, flux and mass distributions will be different compared to Sn. Both of these in turn are also different from the standpoint of contamination given that both are metallic impurities and Xe is an inert gas. The former will lead to deposition of material on the mirror surface. In the case of Xe, thermal deposition would be absent however the energetic Xe implantation on the mirror surface could lead to inert gas damage such as surface blistering and gas bubble production for large doses. Debris mitigation systems would have to be designed according to the radiator used.

3. EUV radiation-driven plasmas

As discussed earlier, Figure 1 shows the general configuration of a DPP system for EUV 13.5-nm light generation. Another "coupling" effect of the DMZ in the source system (e.g. from the electrode materials of the source through the DMZ to the collector mirror) is the fact that the intense EUV and UV radiation generated from the 13.5-nm radiators (e.g. Xe or Sn) can induce a secondary low-temperature plasma at the surface of the collector mirror by ionizing the protective gas used for debris mitigation such as argon or helium [Van der Velden et al, 2006, Van der Velden & Lorenz, 2008]. The characteristic plasma in this region is found to be of low temperature (e.g. 5-10 eV) and moderate densities (e.g. ~ 10^{16} cm^{-3}). The photoionization process can lead to fast electrons that induce a voltage difference the order of 70 V. In addition, due to the sheath region at the plasma-material interface between the plasma and the mirror the ionized gas particles (e.g. Ar^+ or He^+) can be accelerated up to about 50-60 eV. This energy in the case of Ar ions is relatively low and in the so-called sputter threshold regime for bombardment on candidate collector mirror material candidates. In addition, carbon contamination could also be accompanied by this plasma exposure. These candidate materials are typically thin (~20-60 nm) single layers of Ru, Rh or Pd, all of which reflect 13.5-nm light very efficiently. Only few studies have been conducted to elucidate how these low-energy ions may induce changes that can degrade the optical properties of the 13.5-nm collector mirrors. Van der Velden and Allain studied this effect in detail in the *in-situ* experimental facility known as IMPACT to determine the sputter threshold levels at similar energies [Allain et al, 2007]. In the work by van der Velden et al. the threshold sputtering of ruthenium mirror surface films were found to be in close agreement with theoretical models by Sigmund and Bohdansky. The sputter yields varied between 0.01-0.05 atoms/ion for energies about 50-100 eV and models were found to be within 10-15% of these values.

4. Irradiation-driven mechanisms on material surfaces

Before discussion of collector mirror geometry and configuration a brief background on irradiation-driven mechanism on material surfaces is in order. In DPP EUV devices electrodes at the source are exposed to short (10-20 nsec) high-intensity plasmas leading to a variety of erosion mechanisms. Erosion of the electrodes is dictated by the dynamics of the plasma pinch for configurations such as: dense plasma focus, Z-pinch and capillary. The transient discharge deposits 1-2 J/cm^2 per pulse on electrode surfaces. Large heat flux is deposited at corners and edges leading to enhanced erosion. Understanding of how particular materials respond to these conditions is part of rigorous design of DPP electrode systems. Erosion mechanisms can include: physical sputtering, current-induced macroscopic erosion, melt formation, droplet, and particulate ejection [Hassanein et al, 2008]. Erosion at the surface is also governed by the dynamics of how plasma can generate a vapor cloud leading to a self-shielding effect, which results in ultimate protection of the surface bombarded. Determining whether microscopic erosion mechanisms such as: physical sputtering or macroscopic mechanisms such as melt formation and droplet ejection the dominant material loss mechanism remains an open question in DPP electrode design. This is because such mechanisms are inherently dependent on the pinch dynamics and operation of the source. One important consequence of the extreme conditions electrode and collector optics surfaces are exposed is the existence of several irradiation-driven mechanisms that can lead to substantial materials mixing at the plasma-material interface. Bombarment-induced modification of materials can in principle lead to phase transition mechanisms that can substantially change the mechanical properties of the material accelerating degradation.

Conceptually, the phenomenon of bombardment-induced compositional changes is simplest when only athermal processes exist such as: preferential sputtering (PS) and collisional mixing (CM). Preferential sputtering occurs in most multi-component surfaces due to differences in binding energy and kinematic energy transfer to component atoms near the surface. Collisional mixing of elements in multi-component materials is induced by displacement cascades generated in the multi-component surface by bombarding particles/clusters and is described by diffusion-modified models accounting for irradiation damage. Irradiation can accelerate thermodynamic mechanisms such as Gibbsian adsorption or segregation (GA) leading to substantial changes near the surface with spatial scales of the order of the sputter depth (few monolayers). GA occurs due to thermally activated segregation of alloying elements to surfaces and interfaces reducing the free energy of the alloy system. Typically, GA will compete with PS and thus, in the absence of other mechanisms, the surface reaches a steady-state concentration approaching that of the bulk. However when other mechanisms are active, synergistic effects can once again alter the near-surface layer and complex compositions are achieved. These additional mechanisms include: radiation-enhanced diffusion (RED) due to the thermal motion of non-equilibrium point defects produced by bombarding particles near the surface, radiation-induced segregation (RIS), a result of point-defect fluxes, which at sufficiently high temperatures couples defects with a particular alloying element leading to compositional redistribution in irradiated alloys both in the bulk and near-surface regions. Figure 4 shows the temperature regime where these mechanisms are dominant. All of these mechanisms must be taken under account in the design of proposed advanced materials for the electrodes and the collector optics in addition to considering other bombardment-induced

conditions (i.e., clusters, HCI, neutrals, redeposited particles, debris, etc…) that can be generated at the 13.5-nm light tool.

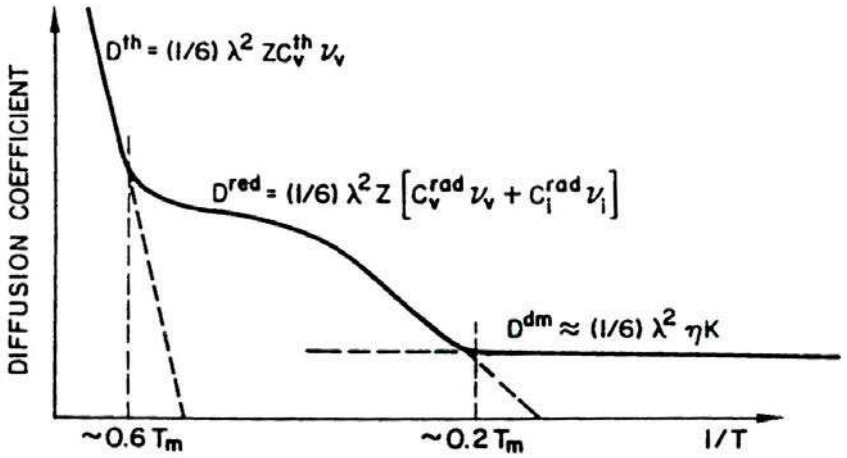

Fig. 4. Schematic plot of the relative importance and temperature dependence of displacement mixing, radiation-enhanced and thermally-activated mechanisms (e.g., Gibbsian segregation).

Modeling of physical sputtering is well known and the field quite mature, see for example work by W. Eckstein (Eckstein 1991) and W. Möller (Möller 1988). For energies above about 100 eV, binary collision approximation (BCA) codes are often used to estimate erosion from various material surfaces. The sputtering yield of 100% Cu from 1 keV Xe^+ bombardment coincides with the experimental result shown for Cu bombardment. Furthermore, example in Figures 5a and 5b, the sputtering from a W-Cu alloy is modeled. The advances in multi-scale and multi-component modeling provided by Monte Carlo damage codes such as TRIM-SP, TRIDYN and ITMC enables scoping studies of candidate materials and their surface response.

An additional mechanism currently missing in plasma-material interaction computational codes is the correlation of surface morphology with surface concentration. Ion-beam sputtering is known to induce morphology evolution on a surface and for multi-component material surfaces plausibly driven by composition-modulated mechanisms [Carter, 2001; Muñoz-Garcia et al., 2009]. Chason et al. have devised both theory and experiments to elucidate on surface patterning due to ion-beam sputtering [Chan & Chason, 2007]. A number of efforts also are attempting to enhance the ability to model ion-irradiation induced morphology and surface chemistry including work by Ghaly and Averback using molecular dynamics and by Heinig et al. using MD coupled KMC (kinetic Monte Carlo) approaches [Ghaly et al, 1999; Heinig et al., 2003]. In spite of these efforts there remains outstanding issues in ion-beam sputtering modification of materials such as the role of mass redistribution that can dominate over surface sputtering mechanisms [Aziz, 2006; Madi et al., 2011]. These developments have important ramifications to the EUV collector mirror operation given the complexity of energetic and thermal particle-surface coupling.

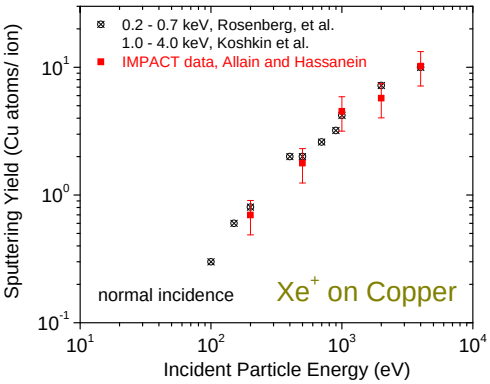

Fig. 5a. Sputtering yield of copper bombarded by singly-charged xenon at normal incidence in the IMPACT (Interaction of Materials with charged Particles And Components Testing) experiment at the Argonne National Laboratory.

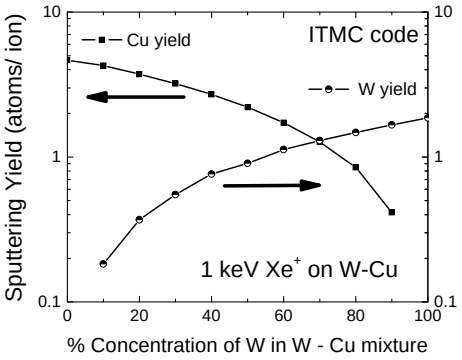

Fig. 5b. The Ion Transport in Materials and Compounds code developed at the Argonne National Laboratory calculates the partial sputtering yield of Cu and W from a W-Cu mixed material bombarded by 1 keV Xe ions at normal incidence. This system is used as a pseudo-alloy with properties able to withstand large heat fluxes in EUV source devices.

5. Collector mirrors for EUV lithography

The nature of the collector mirror damage is largely dictated by the configuration designed to optimize collection of the 13.5-nm light. Due to the refractive index in the X-ray and EUV range being less than unity, total external reflection is possible at angles that are large with respect to the mirror surface plane. If the geometry for collection of the light is such that the mirrors must collect light at more grazing incidence, than the configuration consists of collector mirrors with very thin single-layer coatings of candidate materials such as Ru, Pd or Rh. As discussed earlier the configuration in current EUV source technologies consist of either normal incidence mirrors or grazing incidence mirrors. The latter configuration must use a collection of multiple shell collectors designed to optimize collection of the 13.5-nm

light. Media Lario, a lens manufacturer based in Italy, has optimized the multiple shell collector design in recent years.

5.1 Normal incidence mirrors

The normal incidence mirror configuration consists of a multi-layer mirror geometry exposed to 13.5-nm at normal incidence to the mirror surface. Due to the low reflectance fractions at normal incidence 10's of bilayers are stacked on top of each other to improve the reflectivity to the order of 50-60%. The mechanisms of radiation-induced damage depend on the mirror configuration as eluded above. In the case of the multi-layer mirror (MLM) the incident radiation is predominantly at near-normal incidence thus with the highest projected range into the material bulk. Intrinsic in the configuration of MLM collector systems is the inherent energy distribution of energetic particles that emanate from the LPP pinch plasma source. Although it is not a necessary requirement that MLM are used with LPP sources, the limited collection efficiency of grazing incidence mirrors motivate their use. However, in the context of irradiation damage from the nearby plasma MLM systems suffer the greatest losses in optical performance compared to GIM. The reason is two-fold. One the energy distribution from LPP sources tends to be dominant in the keV range of energies typically about 0.5-5-keV. Therefore there is immediate damage and ion-induced mixing at the MLM interfaces critical to the optimum reflectance of these mirrors. The use of Xe or Sn radiators also introduces a second challenge.

5.2 Grazing incidence mirrors

Grazing incidence mirrors are collector mirrors that reflect EUV light at angles that are predominantly inclined along the plane of the mirror surface. Since the collector mirror will have an inherent curvature the incident angle on the surface plane will have a variable incidence angle depending on the sector the light is collected. Furthermore, recent developments in grazing incidence mirror technology (e.g. Media Lario designs) have now optimized grazing incidence mirrors as shells with a hyperbolic, parabolic or elliposoidal geometric curvature that optimizes the light collection. Typically the collector angle is about 5-25 degrees from the surface normal. In the grazing incidence mirror configuration there exists a number of issues in the context of irradiation-induced effects. For example the sputter efficiency of materials increases as the angle of incidence becomes more oblique. Therefore with this configuration there is the concern that the mirror could erode more rapidly. On the other hand, the implanted energetic debris is found closer to the surface, which could in some cases prove to be of benefit. The issue of incidence angle and its impact on both sputtering of the mirror material and the effect on EUV 13.5-nm reflectivity is discussed in later sections. Grazing incidence mirrors also entail only single layer materials in general. This is because the inherent light transport is via reflection and at grazing incidence typically a large fraction (> 60-70%) of the light can be reflected by materials such as: niobium, rhodium, ruthenium and palladium.

6. Irradiation modification of EUV optical properties

During a Sn-based LPP or DPP pinch, metal vapor will expand and reach nearby components including the collector mirror. Sn+ energies ranging from several hundred electron volts up to a few keV can be expected from Sn-based LPP or DPP source

configurations and therefore constitute the energy range of interest for EUV collector mirror damage evolution. In the years between 2004 and 2007 Allain et al. conducted a series of pioneering experiments at Argonne National Laboratory. The work included a systematic *in-situ* characterization study in IMPACT of how candidate EUV mirror surfaces evolved under exposure to thermal and energetic Sn. Fig. 6 below depicts the various interactions relevant to the EUV 13.5-nm light source environment with candidate grazing incidence mirror materials: Ru, Pd or Rh. In this section studies on these materials and also candidate multi-layer mirror (MLM) materials are discussed with implications of ion-induced damage.

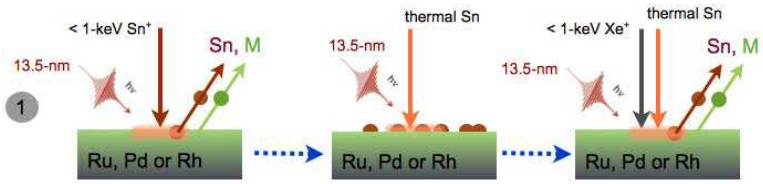

Fig. 6. Schematic of various interactions studied in IMPACT using Sn thermal and energetic particles while *in-situ* characterizing the evolving surface.

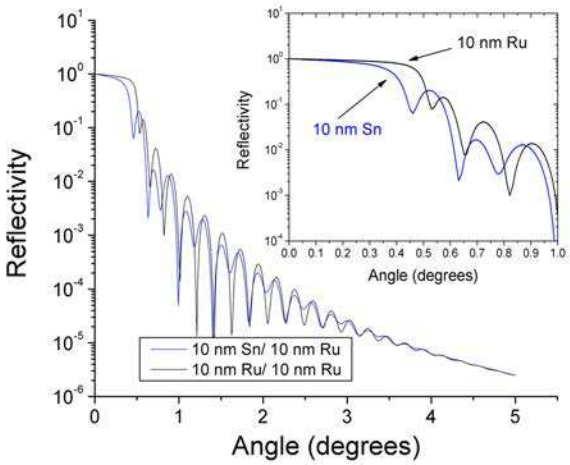

Fig. 7. X-ray reflectivity (8.043 keV X-rays) theoretical response for two different top surfaces: a 10-nm Sn surface on a 10-nm Ru underlayer and a 10-nm Ru surface on a 10-nm Ru underlayer, both with 0.5-nm rms roughness value (CXRO calculations).

The mirror reflectivity response at 13.5-nm light will be sensitive to the thickness of the deposited Sn layer. In addition, the reflectivity response may also be influenced by the structure of the material namely: evaporated porous structure, ion-induced densification phases and possible oxidation effects. All of these can be studied using XRR and in-band EUV reflectivity. When comparing for example a thin Sn layer to a thin Ru layer, theoretically, with enough Sn deposited, the extension of the critical edge will be reduced in the XRR response using CuKα X-rays.

Note the comparison made in Figure 7 showing CuKα (8.043 keV) X-ray reflectivity calculations using CXRO calculations for 10 nm Sn/Ru and 10 nm Ru layers with 0.5 nm rms roughness vs. incident grazing angle [Henke et al, 1993]. In the XRR vs. θ plot, the reflectivity suddenly decreases as θ^{-4} at angles above the critical angle, θ_c, which in this case it is equal to 0.45 degrees and 0.35 degrees for the 10-nm Ru and 10-nm Sn/Ru mirrors, respectively. The presence of the Sn layer effectively reduced the critical edge region and thus its reflectivity performance is reduced. This is because the momentum transfer, Q, is:

$$Q = \left(\frac{4\pi}{\lambda}\right)\sin\theta \tag{1}$$

And the reflectivity response is related by:

$$Q_c^2 = 16\pi\rho_e \propto |R| \tag{2}$$

This reflectivity response can also be assessed for the EUV spectral region (in-band 13.5-nm). Figure 8a shows CXRO calculations of the EUV in-band reflectivity response for same conditions in Figure 7. Note the reduction of the critical edge for the case of Sn deposition with a 10-nm Sn layer on top of a 10 nm Ru SLM.

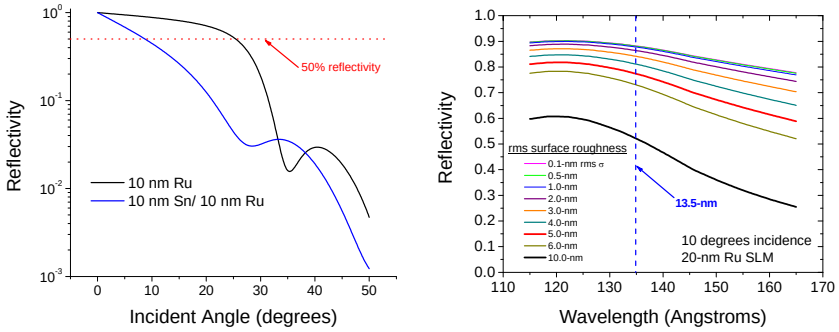

Fig. 8. (a) In-band EUV (13.5-nm) reflectivity response for a 10-nm Ru mirror and same mirror with a 10-nm Sn cap, and (b) theoretical calculations (CXRO) of in-band EUV reflectivity response versus incident angle at 13.5 nm (92 eV) for Ru and Sn surfaces.

Figure 8b shows the effect that surface roughness (e.g. morphology) can have on the absolute in-band (11-17 nm) EUV reflectivity from a 20-nm mirror Ru film surface. This is a great example of how both multi-component surface concentration (e.g. Sn particles in a Ru mirror surface) can couple with surface morphology evolution during deposition. Both a concentration of Sn and surface roughness can combine to decrease the reflectivity near 13.5-nm. The key question is what is the threshold for damage and can this be mitigated so that in steady-state a tolerable and minimal loss of reflectivity can be managed.

Figure 9 show AES data on a thin Ru-cap MLM before and after exposure to Sn vapor in IMPACT, respectively. In-situ metrology in IMPACT allows us to monitor in real time deposition of Sn on the mirror surface. EUV reflectivity from a MLM is near normal and thus the effect of a thin Sn layer must also be assessed as was done for the grazing incidence

mirror data above. Figure 9b shows two major contaminants on the near surface (down to about 50-100 Å), oxygen and nitrogen.

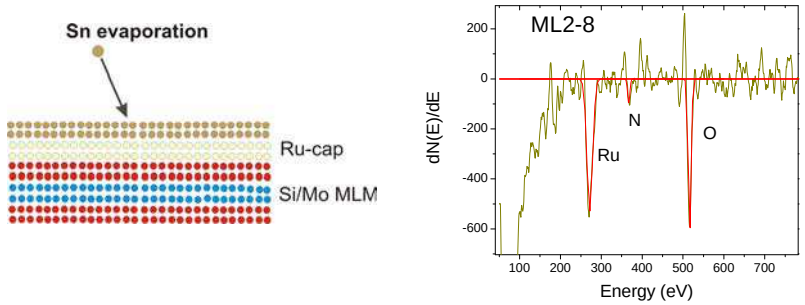

(a) (b)

Fig. 9. (a) Schematic of Sn on MLM system. (b) Auger spectra of a thin Ru-cap MLM showing the presence of oxygen on the thin-film Ru cap. This MLM system can reflect up to about 69-72% of EUV light even in the presence of oxygen.

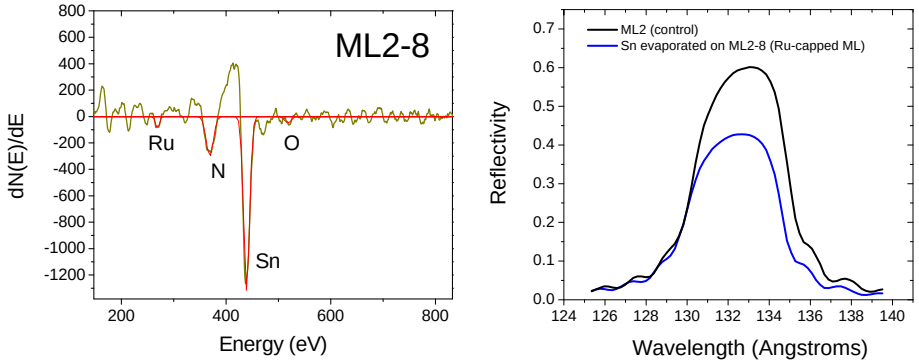

(a) (b)

Fig. 10. (a) Auger spectra of a thin Sn layer evaporated on a thin Ru-cap mirror. Note the presence of nitrogen as opposed to oxygen and the strong Sn peak and (b) In-band EUV reflectivity data taken at NIST-SURF facility. Note the noticeable effect on the reflectivity response for the ML2-8 sample.

Oxygen is always found on the surface in the presence of ruthenium due to its high oxygen affinity. When a thin layer of Sn is deposited as shown in Figure 10a, the major contaminant is nitrogen and not oxygen. This is due to tin's high affinity for nitrogen compared to oxygen. Figure 10b shows the effect of an evaporated Sn layer on EUV mirror reflectivity. The EUV in-band reflectivity was measured at the NIST-SURF facility at near-normal incidence. The reduction from about 60% in-band EUV reflectivity to about 40% is consistent with deposition of about a 40-50 Å Sn thin layer. This has been corroborated by calculations on a thick Ru surface layer at near-normal incidence, giving a thickness comparable to about 35 Å.

6.1 Effect of surface roughness on 13.5-nm reflectivity

The effect of the surface evolution (e.g. concentration and morphology) on 13.5-nm reflectivity is a key factor in determining the lifetime of the collector mirror during operation of the high-intensity EUV lamp. A number of *in-situ* characterization studies are conducted to study the evolution of the surface structure, concentration and morphology under relevant EUV light generation conditions. Single-effect studies are presented in this section to illustrate and differentiate effects from the expanding thermal Sn plume and the energetic Sn particles that emanate from the high-density pinch Sn plasma region.

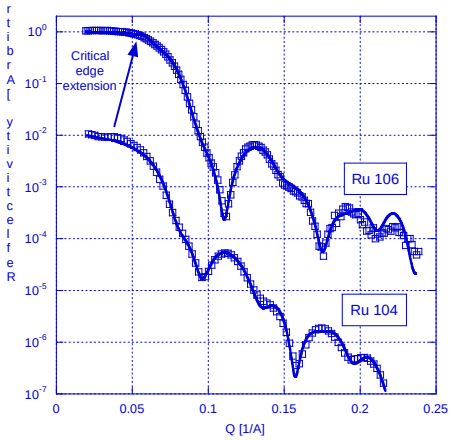

Fig. 11. Fits to Ru 106 and Ru 104. The Ru 104 data set and fit have been shifted downward by a factor of 100 for clarity. The electron density depth profiles from these fits are shown in Figure 12.

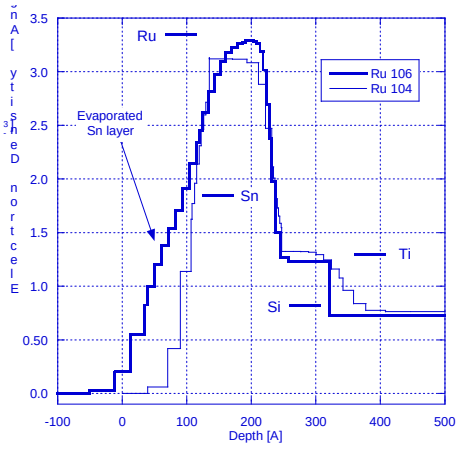

Fig. 12. Electron density profiles for Ru 106 and Ru 104. The presence of a rough Sn layer at the air-film interface of Ru 106 is clear. The bulk density values are shown as horizontal lines.

Fits to Ru 106 (with evaporated Sn layer) and Ru 104 (identical to Ru 106, but without Sn layer) are shown in Figure 11. The electron density depth profiles obtained from these fits are shown in Figure 12. First, the electron density values for Ru 106 and Ru 104 are consistent with the known bulk values. The presence of the Sn layer on Ru 106 is clear. In fact the point at which the profiles for Ru 106 and Ru 104 diverge (near the air-film interface) corresponds to the bulk Sn electron density value. Thus, the Ru 106 data set is consistent with a Sn over-layer approximately 60 Å thick. The air-Sn layer interface is not well defined as determined by the fit of the XRR data. The extension of the critical edge for Ru 106 is evident, an effect due to the Sn layer increasing the total electron inventory of the metal over-layer.

The evaporated Sn layer on this sample is either very rough, has significant internal porosity, or has intermixed with the Ru layer to a large extent. Surface roughness values above 5-nm rms would need to exist to lead to any significant decrease on in-band EUV reflectivity (as shown earlier in Fig. 8b). Significant intermixing is very possible during the low-energy room temperature evaporation. It is possible Sn does not wet Ru adequately and this could lead to a poor surface topography and a rough interface. The blurry Ti-Si interface for the Ru 104 sample probably is not a real effect, but a consequence of an incomplete fit.

The effect of the thin-film Sn layer on in-band (13.5-nm) EUV reflectivity is shown in Figure 13. Measurements were conducted at the NIST-SURF facility. The figure shows two primary cases. One is Ru-104, a virgin 10-nm Ru sample. Both XRR and QCM-DCU (quartz crystal microbalance dual-crystal unit) measurements of this particular batch of Ru SLM measured a Ru film thickness of about 100 Å [Allain et al, 2007]. The EUV in-band 13.5-nm reflectivity data fitted with CXRO calculations is yet a third indication of the Ru thin-film thickness, thus effectively calibrating the QCM-DCU data in *in-situ* characterization. The EUV reflectivity results show that the Ru thin-film thickness is about 90 Å fitting with the CXRO calculations. The sample covered with Sn (Ru-106) is fitted with CXRO calculations using a 2.1-nm Sn surface layer at 20-degrees incidence. This correlates well with estimates from Sn fluences measured in IMPACT giving about a 30-40 Å Sn thin-film layer.

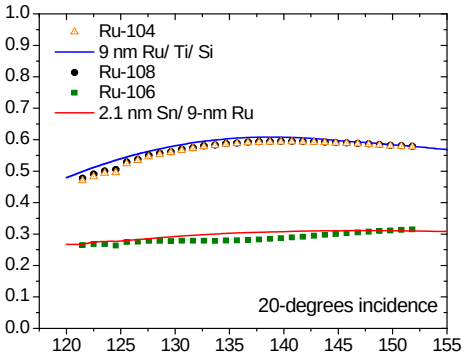

Fig. 13. Two virgin samples, Ru-104 and Ru-108 are shown with their reflectivity response in the EUV in-band 13.5-nm spectral range at 20-degrees with respect to the mirror surface. The reflectivity response of the Sn-covered mirror is also shown.

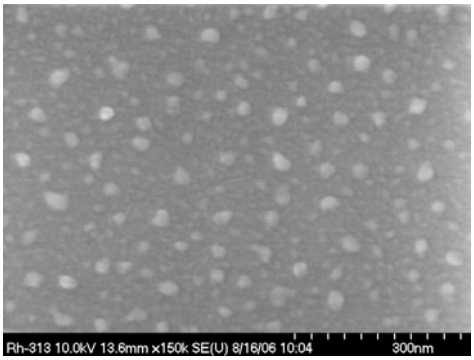

Fig. 14. SEM image of Rh-313 exposed to similar conditions as sample Ru-106. Therefore Sn coverage is equivalent to about a 2-nm thickness of Sn atoms.

The EUV reflectivity mirror response measured in-situ is correlated to ex-situ surface morphology data using SEM and EDX for electron-based microscopy. Fig. 14 shows SEM data for the case of Rh-313 exposed to 50 nA of Sn evaporation for 15-minutes. The surface morphology is characterized by surface structures that vary in lateral size from 10-100 nm. Observations from BES (backscattering electron spectroscopy) data suggested that the lighter imaged structures correspond to Sn, while darker regions corresponded to Rh. This led to the conclusion that the surface structures are islands of Sn that have coalesced during deposition. The formation of these two-dimensional nanostructures could be associated with diffusion-mediated aggregation of deposited Sn atoms. This is partly due to deposition of tin driving the morphology and structure of the Sn film deposited on the SLM surface far from equilibrium conditions. When one incorporates the kinetic effect of energetic implanted Sn, the net energy available is increased dramatically. This point is further investigated in later sections. The formation and growth of nano-scale tin islands during exposure is a competition between kinetics and thermodynamic equilibrium of deposited Sn atoms on the surface of either of the noble metal used (e.g. Ru or Rh).
The results from a set of thin Ru films exposed to energetic Sn ions are shown in Figure 15. The SLD profiles exhibit the effect of sputter erosion caused by the Sn-ion bombardment. Although the fluence of Ru102 and Ru105 differed by a factor of approximately 20, the profiles are similar. This is probably the effect of greater sputter efficiency for the low fluence Ru 105 case where the ion irradiation angle was 45^{o} instead of normal incidence.

6.2 Effect of fast and thermal particles on MLM reflectivity at 13.5-nm

For MLM systems, Xe^{+}-bombardment studies in IMPACT demonstrated that the main failure mechanisms were: 1) ion-induced mixing at the interfaces along with significant sputtering of cap material (i.e., Ru) and 2) synergy of energy (1-keV) and high mirror temperature (200° C) leading to mirror reflectivity degradation [Allain et al., 2006]. Therefore, from the point of view of ion-induced damage, MLM systems compared to SLM systems are most susceptible to early failure rates if fast ion and neutral energies are maintained at the 1 keV level or more.

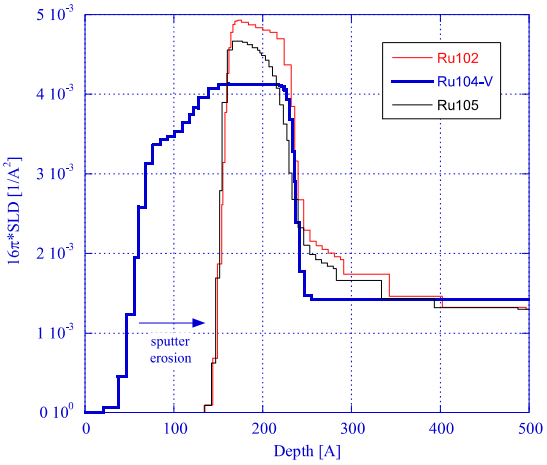

Fig. 15. Electron density depth profiles (ordinate is equal to 16πSLD, where SLD=$r_e\rho_e$, and r_e and ρ_e are the classical electron radius and electron number density, respectively). The overall film thickness for Ru102 and Ru105 has been reduced by sputtering.

Kinematically, Xe and Sn behave similarly, since their mass is very close. However, there is a fundamental difference: unlike Xe (which is inert), Sn can be incorporated into the mirror structure and easily build up on the target. Sn accumulation would be exacerbated if any type of chemical bonding or new phase is formed. The accumulation of Sn is limited during Sn bombardment due to self-sputtering; therefore a steady-state Sn content in the sample is reached. In addition, the overall ion-induced sputtering of the mirror is reduced, since ion-induced sputtering is now shared between the mirror material (i.e., Ru, Rh or Pd) and the previously implanted Sn. Results from Monte Carlo modeling of Sn implantation have shown these trends, and they were later verified by experimental measurements [Allain et al., 2006]. Tests therefore conducted with Xe+ served as an appropriate surrogate for Sn irradiation. Furthermore, since some EUV light sources could in principle use Xe as a 13.5-nm radiatior, these tests were also directly relevant. One particular interesting effect of inert ions such as Xe is that they implant at the near surface and could, if enough vacancy-induced voids are created, lead to Xe bubble accumulation. The work by Allain et al. in fact now has indicated that for a given Xe fluence threshold at 1-keV the stability of small nm-sized bubbles can be created at the near surface of MLM Si/Mo systems. This was indicated by use of XRR tests showing Porod-like scattering of small-angle X-ray scattering experiments.

6.3 Effect of fast and thermal Sn particles on single-layer reflectivity at 13.5-nm

6.3.1 Thermal Sn

Operation of Sn-based EUV lithography DPP sources exposes the collector mirror to two types of Sn contamination: thermal deposition of Sn vapor and bombardment of Sn ions from the expanded plasma. Even with the implementation of debris mitigation mechanisms, some contamination will reach the collector mirror. In the *in-situ* expeirments presented here, both sources of Sn (i.e., energetic and thermal) can be studied on small mirror samples. An electron beam evaporator loaded with Sn supplies the

thermal flux. The energetic Sn flux comes from a focused Sn-ion source. Integration of an *in-situ* EUV reflectometer allows monitoring of the reflectivity in real time as the mirror is exposed to Sn.

EUV reflectivity measurements were monitored as the Sn layer was deposited. Results from these Sn exposures are shown in Figure 16. The lower axis corresponds to the Sn fluence and the thickness of the deposited Sn layer (calculated assuming that the film density is equal to the Sn bulk density) in the upper axis. For the case of the Rh sample (Rh-211) the Sn layer thickness is calculated based on fits with the reflectivity code and absolute at-wavelength 13.5-nm data from NIST. For a 15 nA current on an ECN4 evaporator for 2 minutes, sample Rh-213 was used as calibration sample with similar conditions to Rh-211. The sputter rate measured was 0.048 nm/sec or 2.9 nm/min. For Rh-211, the current level used was 5 nA for 34 minutes. This results in a deposition rate of 0.125 nm/min (2.9 divided by a factor of 3 and 7.75) and multiplied by 34 minutes results in a thickness of about 4.25 nm. Ex-situ XRF measurements resulted in an equivalent Sn thickness of 3.14 nm. The result appears consistent between the independent XRF measurement and the known deposition rate measured in the *in-situ* experiments in IMPACT. However, there are two observations with this result when one examines Fig 16 more carefully. One is the fact that the surface atomic fraction never reaches 100% of Sn atoms to Rh for Rh-211. Since LEISS is sensitive only to the first monolayer and the thickness measured is about 4-nm, one would expect LEISS to only scatter from Sn atoms at the surface. The LEISS data shows that instead an equilibrium concentration is reached near 70%. The second issue pertains to the in-situ relative reflectivity measured. For levels of 4-nm Sn deposition one would expect the relative reflectivity loss is of order 40-50% losses. However, the measurements show that losses in reflectivity are only about 20-30%. This is in direct contradiction to theoretical results of a Sn 4-nm layer on Rh. To investigate this further, a different mirror substrate (Pd) is used with similar Sn exposure conditions.

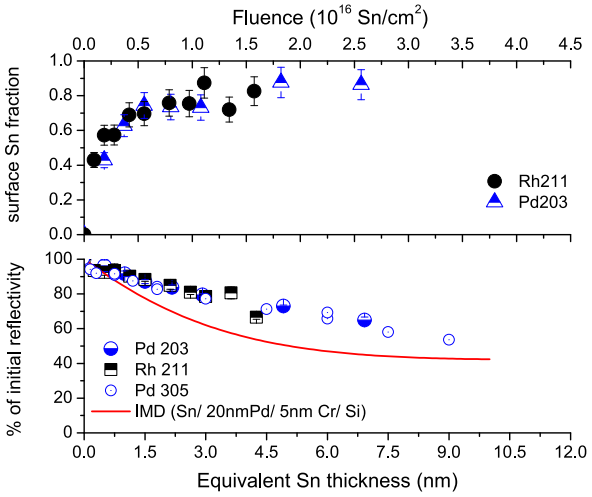

Fig. 16. Evolution of the EUV reflectivity for a Rh mirror as a Sn layer is deposited on the surface compared to deposition on a Pd mirror.

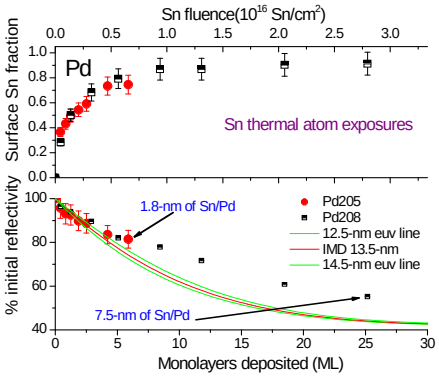

Fig. 17. Evolution of the EUV reflectivity for two Pd mirrors as a Sn layer is deposited on the surface.

Sn thermal deposition on Pd mirrors show similar behavior using about 10 nA of Sn thermal current. This corresponds to a deposition rate of 0.25 nm/min on Pd-203 (2.9 divided by a factor of 1.5 and 7.75) and for a 28 minute exposure a Sn thickness of about 7.5 nm. The XRF measurements resulted in a 6.46 nm equivalent Sn thickness, in reasonable agreement with IMPACT deposition rate measurements. In Figure 16 the relative reflectivity loss is about 35% for Pd-203, much lower than theoretically predicted for deposition of a 7.5-nm Sn layer on Pd.

For the cases of Pd 205 and 208, the deposition rate is 4-5 times less than for Pd-203. This is based on the time of equilibration of the Sn surface atomic fraction measured by LEISS of Pd 205 and 208 compared to Pd 203. Therefore, the deposition rate for Pd 205 and Pd 208 is about 0.0625 nm/min. For Pd-208 and 120 minute exposure the Sn thickness is 7.5 nm and for Pd 205, 28-minute exposure, 1.8 nm. The relative reflectivity losses are 20% and 45% for Pd-208 and Pd-205, respectively as shown in Figure 17. The surface atomic fraction of Pd-208 reaches 85-90% after close to 10^{16} Sn/cm^2 fluence. Before this time, for fluences below 0.6-0.7 x 10^{16} Sn/cm^2 the surface Sn atomic fraction reaches levels of about 70% for Pd-205 and Pd-208 consistent with results for Pd-203. So for exposures below Sn fluences of 10^{16} Sn/cm^2, the relative reflectivity losses are below about 30%. The main difference between Pd-203 and Pd-205, is that for the same exposure time (28 min.), Pd-203 has a "thicker" equivalent Sn layer compared to Pd-205 based on the deposition rate measured. This is an important result in that, although for the fluence exposure one should get "thick" Sn layers, the results from low-energy ion scattering shows otherwise. That is, LEISS is sensitive to the first or second monolayer and the data shows that even in the cases of Pd-203 and Pd-208 about 10-15% of the scattered ions detected, scatter from Pd atoms. Moreover, for lower fluences, scattering from mirror atoms (Pd or Rh) can be as large as 30%. More importantly, the surface Sn fraction seems to reach an equilibrium until the fluence is increased further.

These results imply that Sn is coalescing into nm-scale islands on the substrate surface for Sn exposures below about 10^{16} Sn/cm^2. Surface morphology examination was conducted with scanning electron microscopy (SEM) as a function of the Sn thermal fluence. The results were very important in that it proved that indeed the lower reflectivity loss is attributed to Sn island coalescence.

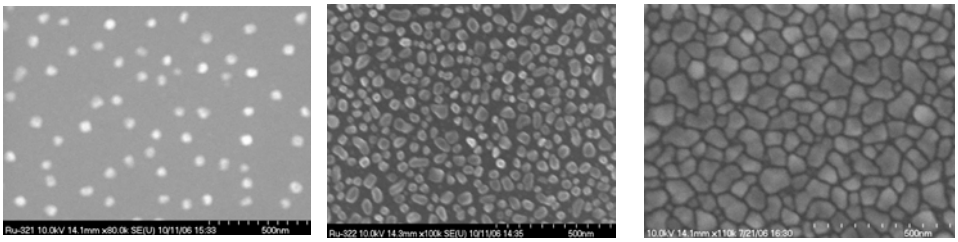

(a) 0.25 x 10^{16} cm^{-2} (b) 1.25 x 10^{16} cm^{-2} (c) 3.0 x 10^{16} cm^{-2}

Fig. 18. SEM micrographs of Sn-deposited Pd thin-film mirrors as a function of the Sn fluence.

6.3.2 Sn ions

EUVL plasma-based Sn sources expose mirrors to both thermal and energetic particles as discussed earlier. In this section we investigate the EUV reflectivity response of grazing incidence mirrors to exposure of Sn ions. The goal of this investigation was to identify failure mechanisms on the performance of Ru mirrors under EUVL source-relevant conditions. Furthermore, these experiments were also designed to elucidate the behavior of energetic Sn particles against results of thermal Sn exposure presented in the previous section. In addition to thermal Sn deposition on the collector mirror in a EUVL source device, the mirror is also subjected to energetic fast-ion and neutral bombardment from expanded plasma that gets through the debris mitigation barrier. The study of this problem is critical to assess the severity of damage induced by fast ion/neutral bombardment on EUV collector mirrors. Ion bombardment induces damage to EUV mirrors with at least three mechanisms: 1) erosion of the mirror material by physical sputtering, 2) modification of surface roughness, and 3) accumulation of implanted material inside the mirror.

These three phenomena have been extensively explored in IMPACT for the case of Xe+ bombardment, both for single-layer and multilayer EUV mirrors (Nieto et al, 2006). For this case, the first mechanism, erosion of the mirror, was determined to be the limiting factor for mirror lifetime. Surface roughness changes induced by ion bombardment in those cases were not large enough to affect the reflectivity in a significant manner. This was consistent with findings of irradiated thin-film surfaces of mirrors fabricated with magnetron sputtering. Typically these films consist of large grain boundary density, and thus surface corrugated structures from ion-beam bombardment are minimized. In regards to accumulation, it was observed that large Xe fluences (>10^{17} Xe^{+}/cm^{2}) delivered over a short period of time caused blistering of the mirror most likely due to the formation of bubbles. Xe fuel accumulation in the mirror layer is not regarded as an issue for sources operating with Xe^{+} at low EUV power operation. Under high-power HVM (high-volume manufacturing) level operation, with Xe as the EUV radiator, it's unclear how large dose exposures might scale. Suffice to say that if the Xe flux is not controlled and maintained at tolerable levels, significant damage to the grazing incidence mirror is likely, mostly from ion-induced sputtering (Nieto et al, 2006).

Two experiments were performed by exposing two Ru mirrors to 1.3 keV Sn beams with a current of 40 -50 nA. The beams were rastered over a 0.25 – 0.3 cm^{2} area, giving a net Sn ion flux of ~ 10^{12} ions cm^{-2} s^{-1}. The mirrors were exposed to this Sn beam for three hours (~104 sec), giving a total fluence of 1016 ions cm^{-2}. Sample ANL-H was manufactured by Philips,

and Ru-208 was manufactured by OFM-APS at ANL. Sample ANL-H was bombarded at 60° incidence, while Ru-208 was bombarded at normal incidence. The results of the exposures are presented in Figure 19a and Figure 19b, which show both the Sn surface concentration (upper panels) and relative EUV reflectivity (lower panels).

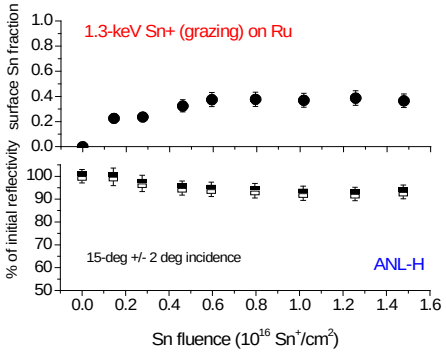

Fig. 19a. Evolution of the surface concentration and the EUV reflectivity of a Ru mirror exposed to a 1.3 keV Sn beam incident at grazing incidence (60°).

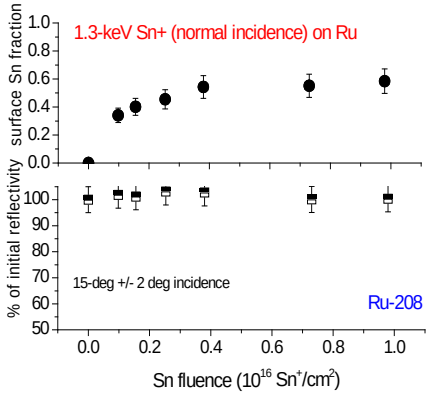

Fig. 19b. Evolution of the surface concentration and the EUV reflectivity of a Ru mirror exposed to a 1.3 keV Sn beam incident at normal incidence (0°).

There are significant differences between the two exposed samples. Regarding the Sn content in the surface, it can be seen that the sample bombarded at grazing incidence (ANL-H) reaches an equilibrium Sn content of 40%, while the sample bombarded at normal incidence has a steady-state Sn surface fraction of 60%. The increase can be explained by an increase of Sn self-sputtering yield. The Sn atomic fraction y_{Sn} on the sample as a function of time is given by:

$$\frac{dy_{Sn}}{dt} = \frac{\Gamma_{sn}}{n_T}\left(1 - y_{Sn}Y_{self\ sp}\right) \tag{3}$$

Equation 3 represents the balance between the implantation and the sputtering flux. The implantation flux is constant, but the sputtered flux is actually a function of the Sn content in the sample, so it gets weighted by the atomic fraction of Sn in the target y_{Sn}. At equilibrium, the time derivative is zero and that condition relates the equilibrium Sn fraction $y_{Sn,eq}$ and the self sputtering yield of Sn, $Y_{self\ sp}$:

$$y_{Sn,eq} = \frac{1}{Y_{self\ sp}} \tag{4}$$

For 60° incidence, the equilibrium fraction is 0.4, which corresponds to a self-sputtering yield of 2.5. For the normal incidence bombardment, the Sn self sputtering yield corresponding to the 0.65 Sn equilibrium atomic fraction is 1.5. These numbers are very close to the ones reported in the literature for Sn self-sputtering. Therefore, this is yet another independent verification of the in-situ EUV reflectivity measurements in IMPACT.
The other interesting observations from [Allain et al, 2007b] and [Allain et al., 2010] relates to the behavior of the EUV reflectivity as Sn is implanted. The effect of implanted Sn is not as drastic as for the case of deposited Sn on the surface, since the change in reflectivity is very small. For the sample irradiated at normal incidence, the reflectivity does not drop at all during the irradiation over a fluence of 10^{16} Sn+/cm^2. For the sample exposed to the beam at 60° incidence, a drop of < 10% in reflectivity is observed. By comparing the fluence scales for figures 18 and 19, it can be seen that the deposited Sn produces a more pronounced drop on reflectivity (15%), a drop at least 3 times larger than the one observed for the samples with implanted Sn. The case for the grazing incidence irradiation produces a larger drop in reflectivity that the normal incidence case, since in the limit of completely grazing incidence (90°), the implantation and thermal deposition cases are basically the same, since there is no penetration into the target.

6.3.3 Sn or Xe ions combined with thermal Sn

To examine the effects of exposure to a more realistic environment in a EUV light tool with both energetic and thermal particles exposing the collector mirror surface, experiments with thermal Sn and energetic Xe^+ were conducted. For these experiments, three samples— Rh 318, Rh 319, and Rh 320 —were each irradiated with a 1 keV ion beam (Xe^+) and exposed to an evaporator (Sn) simultaneously, with a total exposure time of 36 minutes. The target energetic Xe^+ fluences increased by one order of magnitude with each successive sample, beginning at $4.5x10^{15}$ Xe/cm^2, while target thermal Sn fluences remained constant at $4.5x10^{16}$ Sn/cm^2. Two control samples, Rh 321 and Rh 323, were used to compare the effects on reflectivity. Rh 321 was exposed to thermal Sn evaporator with a target Sn fluence of $4.5x10^{16}$ Sn/cm^2 for 36 minutes with no irradiation and Rh 323 was irradiated with an ion beam (Sn^+) at 1.3 keV for 88 mins at a fluence of $1.03x10^{14}$ Sn^+/cm^2 with no thermal Sn deposition.
Figure 20 shows both relative percent EUV reflectivity and Sn surface fraction versus thermal Sn fluence. A direct correlation between reflectivity loss and surface fraction of Sn is observed. Rh 318 and Rh 319 are fully covered with Sn after 3 minutes of exposure and their relative reflectivity decreased by 41.6% and 48.5%, respectively, after 36 minutes. While reflectivity of Rh 318 and Rh 319 decreased as the experiment progressed, Rh 320 had a local maximum at approximately 2.21×10^{16} Sn cm^{-2} where reflectivity increased to 94.7%. The corresponding Xe^+ fluence, 2.25×10^{16} Xe^+ cm^{-2}, exceeds the final fluences for the other two samples. This suggests that Rh 320 reached a threshold—too high for the other samples—

where the surface changed such that reflectivity could reach a maximum. The control sample, Rh 321, behaved extremely similar to Rh 318 and Rh 319 in both the atomic fraction of Sn and relative reflectivity loss. The relative reflectivity of Rh 323 fluctuated with increasing fluence but was found to only decrease 1.4% at the highest fluence, 5.8×10^{15} Sn^{+}/cm^{2}. Figure 5 does not represent the fluence corresponding to the reflectivity of Rh 323 because there was no thermal Sn fluence on the sample. It was plotted purely to show the affects of energetic Sn fluence on reflectivity. The surface fraction of Sn was lowest for this sample when compared to the other Rh samples, which was expected, with the surface fraction of Sn approaching equilibrium at 0.484. This further confirms the direct correlation between reflectivity loss and surface fraction of Sn discussed earlier.

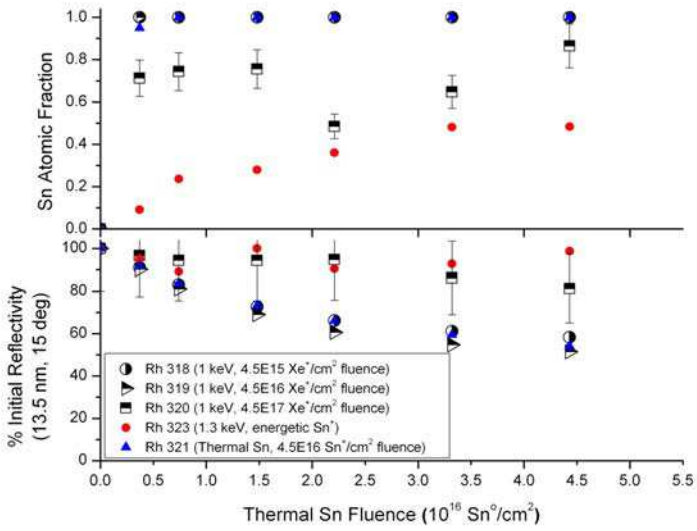

Fig. 20. LEISS data showing the surface Sn fraction versus thermal Sn fluence (top) and 13.5nm EUV reflectivity measurements versus thermal Sn fluence (bottom). Rh 321 had thermal Sn deposition only at a fluence of 4.5E16 Sn^{0}/cm^{2}. The fluence of Rh 323 shown, for both cases, is meant for correlation purposes only since there is no thermal Sn fluence on the sample.

	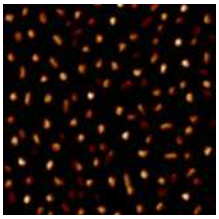 10x10 µm	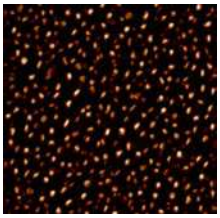 10x10 µm	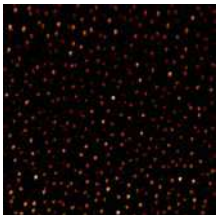 10x10 µm
Sample	Rh 318	Rh 319	Rh 320
Area Ra (nm)	18.5	14.8	2.00
Area RMS (nm)	22.4	19.4	3.20
Average height (nm)	60.9	16.7	1.78
Max. height (nm)	137	100	26.4

Table 1. Two-dimensional (10x10 µm) atomic force microscope (AFM) images and roughness values calculated with the AFM computer analysis program.

	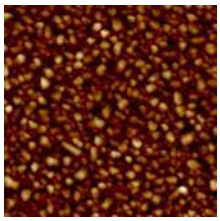 5x5 µm	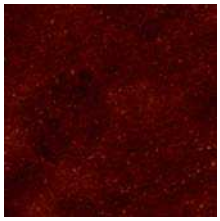 5x5 µm
Sample	Rh 321	Rh 323
Area RMS (nm)	14.12	0.11
Max. height (nm)	89.00	2.05
Feature Area (um^2)	22.98	n/a
Feature Coverage (%)	91.9%	n/a

Table 2. Two-dimensional (5x5 µm) atomic force microscope (AFM) images and roughness values calculated with the AFM computer analysis program for Rh thermal Sn only (left) and energetic Sn only (right) samples.

The AFM investigated the morphology of the samples. Table 1 and 2 illustrate the results. As the fluence of the samples is increased, it is found that the height, the roughness and the general size of the features decrease significantly. This is likely due to the increase in sputtering of Sn caused by the higher Xe^+ fluence. Rh 318 has the largest roughness and height values, at 22.4 nm and 137 nm respectively, but has the lowest fluence of the sample set. Rh 320 on the other hand has the smallest values for roughness and height, 3.20 nm and 26.4 nm, but the largest fluence of the set. This shows a direct correlation between the morphology of the samples and the fluence of Xe^+.

There is also a correlation between the morphology and the resulting reflectivity. For these samples, the lower roughness value (and height value) corresponds to the highest reflectivity. This is seen with Rh 320, where the reflectivity drop is 18.7% and the RMS value for the roughness is 3.20 nm, the lowest value for each in the sample set. For Rh 318 and Rh 319, the roughness values are 22.4 nm and 19.4 nm and the height values are 60.9 nm and 16.7 nm with corresponding reflectivity losses of 41.7% and 48.5%, respectively.

The difference in surface morphology for thermal Sn only and energetic Sn only is clearly illustrated in table 2. The roughness for thermal Sn deposition only, Rh 321, was found to be 14.12 nm, almost identical to Rh 319, 14.8 nm, and very close to Rh 318, 18.5 nm. This closeness is surface roughness, as well as similarities in reflectivity loss and Sn atomic fraction, elucidates the correlation between surface morphology and resulting reflectivity. This is further cemented by comparing the reflectivity loss of Rh 323 with its surface morphology. Rh 323 had a surface roughness of only 0.11 nm and maximum feature height of 2.05 nm with its largest drop in reflectivity being only 11%.

7. Conclusion

In conclusion, the success of EUV lithography as a high-volume manufacturing patterning tool remains elusive although great progress has been made in the past half decade. One main challenge is the plasma-facing components (e.g. electrodes, collector mirrors and debris mitigation shields) lifetime that ultimately impact the EUV power available for exposure.

8. Acknowledgements

We acknowledge the Intel Corporation, Dr. Melissa Shell, Dr. Bryan Rice (currently as an Intel at Sematech SUNY Albany), and Dr. Robert Bristol. We thank our strong collaborations with numerous groups including the groups of: Dr. Charlie Tarrio at NIST, Prof. Brent J. Heuser at University of Illinois, Dr. Peter Zink formerly from Philips Research Labs, Dr. Al Macrander of the Optics Laboratory at Argonne National Laboratory, Dr. Sasa Bajt formerly of Lawrence Livermore National Laboratory, and Dr. Vivek Bakshi formerly of Sematech.

9. References

Allain, J. P.; Hassanein, A. et al, "Effect of charged-particle bombardment on collector mirror reflectivity in EUV lithography devices", Proc. SPIE Int. Soc. Opt. Eng. 6151 (2006) 3

Allain, J. P.; Nieto, M.; Hendicks, M.; Harilal, S. S.; Hassanein, A (2007). *Debris-and radiation-induced damage effects on EUV nanolithography source collector mirror optics performance,* SPIE Proceedings, 6586(2007):22, doi: 10.1117/12.723692

Allain, J.P., Nieto, M., Hendricks, M.R., Plotkin, P., Harilal, S.S, & Hassanein, A (2007). IMPACT: A facility to study the interaction of low-energy intense particle beams with dynamic heterogeneous surfaces. Rev. Sci. Instrum. 78, 113105 (2007), ISSN 0034-6748

Allain, J.P.; Nieto-Perez, M.; Hendricks, M.R.; Zink, P.; Metzmacher, C.; & Bergmann, K. (2010). *Energetic Sn+ irradiation effects on ruthenium mirror specular reflectivity at 13.5-nm.* Applied Physics A, 100, 1, pp. 231-237, (July 2010), ISSN 0947-8396

Allain, J.P.; Nieto, M.; & Hassanein, A. (2008). *Specular reflectivity of 13.5-nm light from Sn islands deposited on grazing incidence mirror surfaces. Applied Physics A*, 91, 1, pp. 13-16, (April 2008), ISSN 0947-8396

Aziz, M. J. (2006). *Nanoscale Morphology Control Using Ion Beams*, Proceeding in Ion Beam Science: Solved and Unsolved Problems, Matematisk-fysiske Meddelelser 52, Sigmund, P. (editor), ISBN: 87-7304-330-3

Bakshi, V. Editor (2006). *EUV Sources for Lithography*, SPIE, Bellingham, WA, ISBN 0819458457

Bakshi, V. Editor (2009). *EUV Lithography*, SPIE and John Wiley & Sons, Hoboken, New Jersey, ISBN 978081946949

Banine, V. & Moors R. (2004). *Plasma sources for EUV lithography exposure tools*, J. Phys. D: Appl. Phys. 37 3207

Banine, V.; Koshelev, K.N.; Swinkels G.H.P.M. (2011) *Physical processes in EUV sources for microlithography*, J. Phys. D: Appl. Phys. 44 253001

Benschop, J.; Banine, B.; Lok, S.; & Loopstra, E. (2008). *Extreme ultraviolet lithography: Status and prospects*, J. Vac. Sci. Technol. B 26, 2204, ISSN 1520-8567

Campos, D.; Harilal, S. S.; & Hassanein, A. (2010). *The effect of laser wavelength on emission and particle dynamics of Sn plasma*, J. Appl. Phys. 108, 113305, ISSN 1089-7550

Carter, G., (2001). *The physics and applications of ion beam erosion.* Journal of physics. D, Applied physics 34.3, doi: 10.1088/0022-3727/34/3/201

Chan, W; Chason E (2007). *Making waves: Kinetic processes controlling surface evolution during low energy ion sputtering*, J. Appl. Phys. 101, 121301, DOI:10.1063/1.2749198

Eckstein, W. Comp*uter simulation of ion-solid interactions,* Springer Series in Materials Science, Vol. 10, Springer, Berlin, 1991, ISBN 3-540-190570-0

Fahy, K.; O'Reilly, F.; Scally, E.; & Sheridan, P. (2010). *Robust liquid metal collector mirror for EUV and soft x-ray plasma sources*, Proceedings Vol. 7802 in Advances in X-Ray/EUV Optics and Components V, Goto, S.; Khounsary, A. M.; & Morawe, C., Editors (2010). 78020K, 27 August 2010, Proc. SPIE 7802, 78020K (2010); doi:10.1117/12.860747

Ghaly, M.; Nordlund, N.; Averback, R.S. (1999). *Molecular dynamics investigations of surface damage produced by kiloelectronvolt self-bombardment of solids*, Philosophical Magazine A, vol. 79, Iss. 4, p.795-820, doi: 10.1080/01418619908210332

Harilal, S. S.; O'Shay, B.; Tillack, M. S.; Tao, Y.; Paguio, R.; Nikroo, A.; & Back, C. A. (2006). *Spectral control of emissions from tin doped targets for extreme ultraviolet lithography*, J. Phys. D: Appl. Phys. 39 484

Hassanein, A.; Sizyuk, V.; and Sizyuk, T. (2008). *Multidimensional simulation and optimization of hybrid laser and discharge plasma devices for EUV lithography,* Proc. SPIE 6921, 692113-1-15, DOI:10.1117/12.771218

Heinig, K.H.; Muller, T; Schmidt, B; Strobel, M.; Moller, W. (2003). *Interfaces under ion irradiation: growth and taming of nanostructures,* Appl. Phys. A, vol. 77, iss. 1, pp. 17-25, ISSN: 0947-8396

Henke, B. L.; Gullikson, E. M.; Davis, J.C. (1993). *X-ray interactions: photoabsorption, scattering, transmission, and reflection at E=50-30000 eV, Z=1-92*, Atomic Data and Nuclear Data Tables, Vol. 54, 181-342, Available from: http://henke.lbl.gov/optical_constants

Jurczyk, B. E.; Vargas-Lopez, E.; Neumann, M. N.; & Ruzic, D. N. (2005). *Illinois debris-mitigation EUV applications laboratory*, Microelectronic Engineering, Volume 77, Issue 2, February 2005, Pages 103-109, ISSN 0167-9317

Madi, C. S.; Anzenberg, E.; Ludwig, K.; Aziz M.J. (2011). *Mass Redistribution Causes the Structural Richness of Ion-Irradiated Surfaces,* Physical review letters 106.6, 66101.

Möller, W.; Eckstein, W.; Biersack, J.P. (1988). *Tridyn-binary collision simulation of atomic collisions and dynamic composition changes in solids,* Computer Phys. Comm. 51, No. 3, 355-368.

Muñoz-Garcia, J; Vazquez, L.; Cuerno, R.; Sanchez-Garcia, J.; Castro, M.; Gago, R. (2009). *Self-Organized Surface Nanopatterning by Ion Beam Sputtering,* in Toward Functional Nanomaterials: Lecture Notes in Nanoscale Science and Technology, Whang, Z (Ed.), Springer-Verlag, pp. 323 – 398, ISBN 978-0-387-77716-0

Nieto, M.; Allain, J.P.; Titov, V.; Hendricks, Matthew R.; Hassanein, A.; Rokusek, D.; Chrobak, C.; Tarrio, Charles; Barad, Y.; Grantham, S.; Lucatorto, T.B.; Rice, B. (2006). *Effect of xenon bombardment on ruthenium-coated grazing incidence collector mirror lifetime for extreme ultraviolet lithography*, J. of Appl. Phys., Vol. 100 Issue 5, p053510, ISSN: 00218979

O'Connor, A.; Dunne, P.; Morris, O.; O'Reilly, F.; O'Sullivan, G.; & Sokell, E. (2009). *Investigation of ions emitted from a tin fuelled laser produced plasma source*, J. Phys.: Conf. Ser. 163 012116

Tarrio, C. & Grantham S. (2005). *Synchrotron beamline for extreme-ultraviolet multilayer mirror endurance testing*, Rev. Sci. Instrum. 76, 056101, ISSN 0034-6748

Thompson, K. C.; Antonsen, E. L.; Hendricks, M. R.; Jurczyk, B. E.; Williams, M.; & Ruzic, D. N. (2006). *Experimental test chamber design for optics exposure testing and debris characterization of a xenon discharge produced plasma source for extreme ultraviolet lithography*, Microelectronic Engineering, Vol. 83, Iss. 3, pp. 476-484, (March 2006), ISSN 0167-9317

Van der Velden, M; Lorenz, M. (2008). *Radiation Generated Plasmas: a challenge in modern lithography,* Technische Universeit Eindohoven, Proefshcrift, ISBN: 978-90-386-1258-4

Van der Velden, M. H. L.; Brok, W. J. M.; van der Mullen, J. J. A. M.; & Banine, V. (2006). Kinetic simulation of an extreme ultraviolet radiation driven plasma near a multilayer mirror, J. Appl. Phys. 100 (7) 073303, ISSN 1089-7550

van Herpena, M.M.J.W.; Klundera, D.J.W.; Soera, W.A.; Moorsb, R.; & Banineb, V. (2010). *Sn etching with hydrogen radicals to clean EUV optics*, Chemical Physics Letters, Vol. 484, Iss. 4-6, Pp. 197-199, (January 2010), ISSN 0009-2614

Vargas López, E.; Jurczyk, B. E.; Jaworski, M.A.; Neumann, M. J.; & Ruzic, D. N. (2005). *Origins of debris and mitigation through a secondary RF plasma system for discharge-produced EUV sources*, Microelectronic Engineering, Vol. 77, Iss. 2, pp. 95-102, (February 2005), ISSN 0167-9317

Wagner, C. & Harned, N. (2010). *EUV lithography: Lithography gets extreme*, Nature Photonics 4, 24 – 26 ISSN 1749-4885

Yoshioka, M.; Teramoto, Y.; Zink, P.; Schriever, G.; Niimi, G.; & Corthout, M. (2010). in Proceedings Vol. 7636, Extreme Ultraviolet (EUV) Lithography, 2010, 763610-1

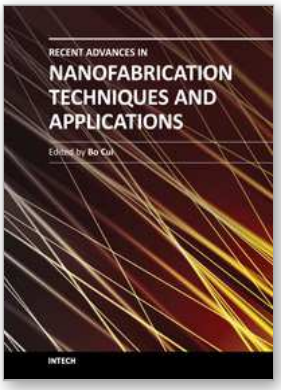

Recent Advances in Nanofabrication Techniques and Applications
Edited by Prof. Bo Cui

ISBN 978-953-307-602-7
Hard cover, 614 pages
Publisher InTech
Published online 02, December, 2011
Published in print edition December, 2011

Nanotechnology has experienced a rapid growth in the past decade, largely owing to the rapid advances in nanofabrication techniques employed to fabricate nano-devices. Nanofabrication can be divided into two categories: "bottom up" approach using chemical synthesis or self assembly, and "top down" approach using nanolithography, thin film deposition and etching techniques. Both topics are covered, though with a focus on the second category. This book contains twenty nine chapters and aims to provide the fundamentals and recent advances of nanofabrication techniques, as well as its device applications. Most chapters focus on in-depth studies of a particular research field, and are thus targeted for researchers, though some chapters focus on the basics of lithographic techniques accessible for upper year undergraduate students. Divided into five parts, this book covers electron beam, focused ion beam, nanoimprint, deep and extreme UV, X-ray, scanning probe, interference, two-photon, and nanosphere lithography.

How to reference
In order to correctly reference this scholarly work, feel free to copy and paste the following:

J.P. Allain (2011). Irradiation Effects on EUV Nanolithography Collector Mirrors, Recent Advances in Nanofabrication Techniques and Applications, Prof. Bo Cui (Ed.), ISBN: 978-953-307-602-7, InTech, Available from: http://www.intechopen.com/books/recent-advances-in-nanofabrication-techniques-and-applications/irradiation-effects-on-euv-nanolithography-collector-mirrors

INTECH
open science | open minds

InTech Europe
University Campus STeP Ri
Slavka Krautzeka 83/A
51000 Rijeka, Croatia
Phone: +385 (51) 770 447
Fax: +385 (51) 686 166
www.intechopen.com

InTech China
Unit 405, Office Block, Hotel Equatorial Shanghai
No.65, Yan An Road (West), Shanghai, 200040, China
中国上海市延安西路65号上海国际贵都大饭店办公楼405单元
Phone: +86-21-62489820
Fax: +86-21-62489821